**COVER SHEET**

Paper Number: **230**

Title: **Computational Study for Size Effect in Composites and Nanocomposites**

Authors: Antonio Alessandro Deleo
Marco Salviato

**ABSTRACT**

An extensive parametric study sweeping both material and geometrical parameters is performed using size effect law (SEL) and Cohesive Zone Modeling (CZM). These simulations and recent experimental results suggest that the cohesive law of composites and nanocomposites is bi-linear and that the Fracture Process Zone (FPZ) may be almost fully developed already for laboratory-sized specimens. As a consequence, the scaling of the fracturing behavior may be influenced significantly by not only the total fracture energy but also the parameters describing the shape of the bi-linear cohesive law. The goal of this work is to formulate a master size effect curve that can be used for quick, yet accurate, estimation of energy and cohesive law parameters that can be used for the design of composite aircraft structures.

**NOMENCLATURE**

| | | |
|---|---|---|
| a | = | crack length |
| $B$ | = | specimen thickness |
| $D$ | = | specimen height |
| $E$ | = | Young's modulus |
| $f_t$ | = | strength |
| g(α) | = | dimensionless energy release rate |
| g'(α) | = | dimensionless energy release rate derivative |
| $G_f$ | = | initial fracture energy (mode I) |
| $G_F$ | = | total fracture energy (mode I) |
| $h$ | = | crack width size |
| $K_{IC}$ | = | fracture toughness |
| $K_1$ | = | kinking stress point for bilinear law |
| $l_{ch}$ | = | Irwin's characteristic length |
| $P_c$ | = | critical peak load |
| $S$ | = | specimen width |
| $t$ | = | cohesive element thickness |

$\alpha$ = normalized effective crack length (a/D)
$\gamma$ = fracture energy ratio ($G_F/G_f$)
$\nu$ = Poisson's ratio
$\sigma$ = stress
$\sigma_Y$ = yielding stress
$\sigma_N$ = nominal stress

## INTRODUCTION

Recent studies and experimental results showed that Linear Elastic Fracture Mechanics (LEFM) underestimates the fracture energy when the Fracture Process Zone (FPZ) size is not negligible compared to the size of the structure [1], [2], [3]. As a consequence, fracturing behavior is not only driven by the total fracture energy, but also by the shape of the cohesive law [4]. This can be explained using Figure 1 below.

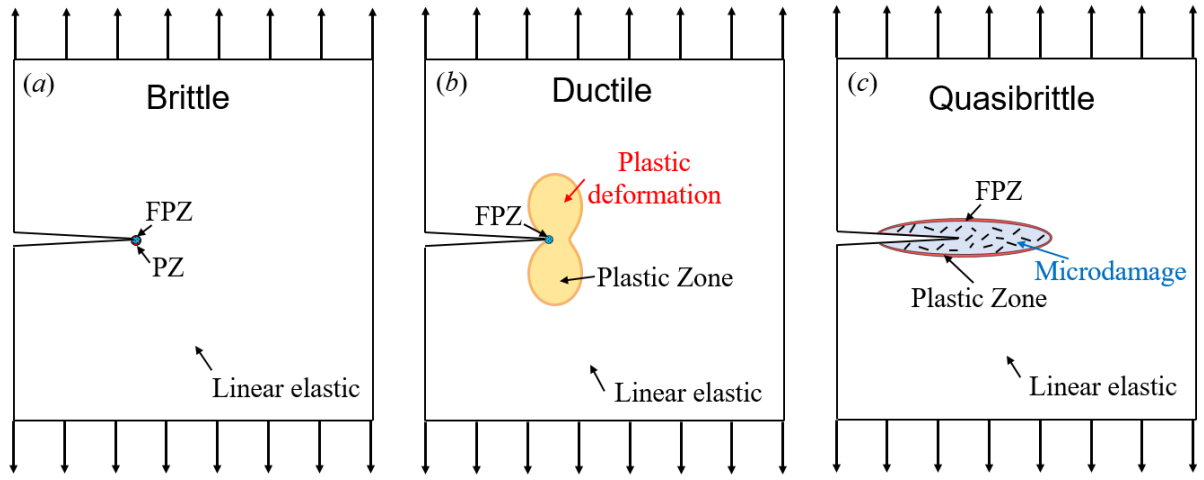


Figure 1 – Differences between Brittle, Ductile, and Quasibrittle materials.

For brittle materials, where the size of the FPZ and Plastic Zone (PZ) is small compared to the structure, LEFM works really well and computational model results generally agree with experiments. For ductile materials, while LEFM cannot be used due to the large plastic zone, the overall behavior is accurately captured by Elasto-Plastic Fracture Mechanics (EPFM) and nowadays it is well-known and widely used. For quasibrittle materials instead, the majority of the nonlinear zone undergoes microdamage and softening and therefore LEFM becomes inapplicable since FPZ is inherently neglected.

A clear example would be in the application of Micro Electro-Mechanical Systems (MEMS devices). While for very large specimen sizes the Fracture Process Zone (FPZ) might be fully developed, meaning that the shape and type of the cohesive traction separation law would not matter at all if not just the total value of the fracture energy, for smaller specimens that might not be true. Therefore, one can only rely on size effect tests and cohesive modeling.

## THEORY AND MODELING

### A. BUCKINGHAM PI THEOREM

Since many parameters are involved and it would not be possible to study and simulate any combination, the form of the function that should be studied was targeted using Buckingham-Π theorem.

Given nine main parameters:

$$\sigma_N, f_t, G_F, G_f, K_1, E, a, D, S, t$$

And two physical quantities:

$$[F], [L]$$

Using $G_F$ and $D$ as fundamentals variables, seven governing dimensionless parameters were found as shown using Eq.(3a) to Eq.(3g).

$$\Pi_1 = \sigma_N G_F^{\alpha} D^{\beta} = \frac{\sigma_N}{G_F} D = \left(\frac{f_t}{\sigma_N}\right)^2 \frac{1}{g'(\alpha)} \qquad Eq.(3a)$$

$$\Pi_2 = f_t G_F^{\alpha} D^{\beta} = \frac{f_t}{G_F} D = \frac{f_t}{E} \qquad Eq.(3b)$$

$$\Pi_3 = G_f G_F^{\alpha} D^{\beta} = \frac{G_f}{G_F} \qquad Eq.(3c)$$

$$\Pi_4 = K_1 G_F^{\alpha} D^{\beta} = \frac{K_1}{G_F} D = \frac{K_1}{f_t} \qquad Eq.(3d)$$

$$\Pi_5 = E G_F^{\alpha} D^{\beta} = \frac{E}{G_F} D = \frac{D}{l_{ch}} \frac{g(\alpha)}{g'(\alpha)} \qquad Eq.(3e)$$

$$\Pi_6 = a G_F^{\alpha} D^{\beta} = \frac{a}{D} \qquad Eq.(3f)$$

$$\Pi_7 = S G_F^{\alpha} D^{\beta} = \frac{S}{D} \qquad Eq.(3g)$$

where $g(\alpha)$ is the dimensionless energy release rate of equivalent LEFM characterizing the specimen geometry, defined below in Eq. (4)

$$g(\alpha) = \frac{E G(\alpha)}{\sigma_N^2 D} \qquad Eq.(4)$$

such that $\alpha = a/D$, and $G(\alpha)$ as the total energy release rate. The quantity for which $G(\alpha)$ is multiplied, $E/\sigma_N^2 D$ characterizes the energy release for a particular geometry. $g'(\alpha)$ is simply the derivative with respect $\alpha$ of the dimensionless energy release rate $g'(\alpha) = dg(\alpha)/d\alpha$.

### B. EQUATION IN PARAMETRIC SPACE

The parameters found above yield a function in a parametric space where Eq.(3a) and Eq.(3e) were chosen to represent the results in a X-Y plot as shown below in Eq.(5) and Eq.(6).

$$X = \frac{D}{l_{ch}} \frac{g(\alpha)}{g'(\alpha)} \qquad Eq.(5)$$

$$Y = \left(\frac{f_t}{\sigma_N}\right)^2 \frac{1}{g'(\alpha)} = f\left(\frac{a}{D}, \frac{S}{D}, \frac{D}{l_{ch}} \frac{g(\alpha)}{g'(\alpha)}, \frac{K_1}{ft}, \frac{G_f}{G_F}, \frac{f_t}{E}\right) \qquad Eq.(6)$$

### C. BILINEAR LAW

It is important to notice that in Eq.(6) $Y$ is a function of both geometrical parameters and bilinear traction separation law parameters. Bilinear cohesive laws can be described using four parameters: $f_t$, $G_F$, $\gamma$, and $K_1$ as shown below in Figure 2.

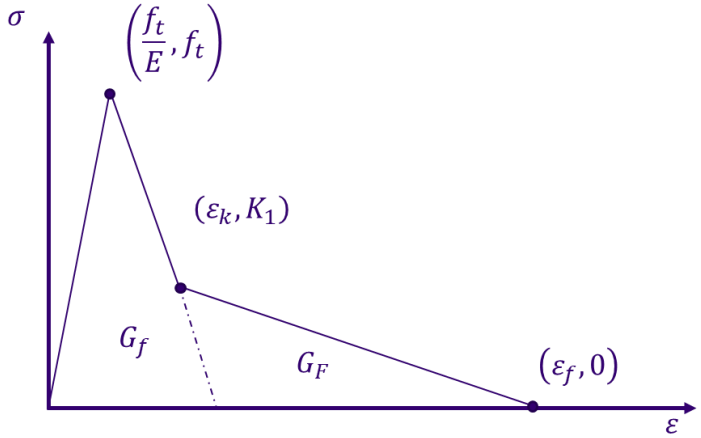


Figure 2 – Example of Bilinear Traction Separation Law

Moreover, if a simple damage model is used to describe the softening behavior as in Eq.(7):

$$\sigma = (1 - D)E \cdot \varepsilon \qquad Eq.(7)$$

Using geometrical construction, the following equations can be derived:

$$D^1(\varepsilon) = 1 - \frac{\left(\varepsilon - \frac{f_t}{E}\right) s_1(\varepsilon) + f_t}{E\varepsilon} \qquad Eq.(8a)$$

$$D^2(\varepsilon) = 1 - \frac{(\varepsilon - \varepsilon_k) s_2(\varepsilon) + K_1}{E\varepsilon} \qquad Eq.(8b)$$

Where $D^1(\varepsilon)$ and $D^2(\varepsilon)$ describe the damage scalar value of each softening branch. For sake of completeness, also the slope of the two branches can be found using Eq.(8c) and Eq.(8d).

$$s_1(\varepsilon) = \frac{K_1 - f_t}{\varepsilon_k - \frac{f_t}{E}} \qquad Eq.(8c)$$

$$s_2(\varepsilon) = \frac{K_1}{\varepsilon_f - \varepsilon_k} \qquad Eq.(8d)$$

Where $\varepsilon_k$, $\varepsilon_f$, graphically shown in Figure 1 are again described using Eq.(9a) and Eq.(9b).

$$\varepsilon_k = \frac{K_1}{E} + 2G_f^* \left(\frac{1}{f_t} - 1\right) \qquad Eq.(9a)$$

$$\varepsilon_f = f_t \left(\frac{\varepsilon_k}{K_1} + \frac{1}{E}\right) + \frac{2G_F^*}{K_1} \qquad Eq.(9b)$$

To eliminate mesh dependency using cohesive elements, the fracture energies must be scaled accordingly to the size of the element chosen. This is shown below in Eq.(10a) and Eq.(10b).

$$G_F^* = G_F^{total} \cdot h^{element} \qquad Eq.(10a)$$

$$G_f^* = G_f^{initial} \cdot h^{element} \qquad Eq.(10b)$$

Eq.(6) to Eq.(10) can fully described any bilinear behavior for any given $\gamma$, but something to keep in mind is that $\varepsilon_k$ must be always greater than $f_t/E$ in order to avoid positive slope for the first softening branch. If this is satisfied, re-arranging Eq.(9a) and Eq.(9b) yields to Eq.(11a).

$$\gamma > \frac{f_t^2}{2EG_F^*} \quad for \quad \varepsilon_k > \frac{f_t}{E} \qquad Eq.(11a)$$

Similarly, assuming that $\varepsilon_k$ has to always be less $\varepsilon_f$, Eq.(11b) can be derived for the limit on the second softening branch:

$$\gamma < \frac{f_t^2[2EG_F^* + K_1(2f_t - K_1)]}{2EG_F^*(f_t - K_1)^2} \quad for \quad \varepsilon_k < \varepsilon_f \qquad Eq.(11b)$$

### D. J-INTEGRAL VERIFICATION

To calculate the dimensionless energy release rate $g(\alpha)$ the J-Integral method [5], using Eq.(12) was used in Abaqus Standard-Implicit 2017. 8-node biquadratic plain strain quadrilateral elements, CPS8 [6], were used together with the quarter element technique [7] to provide accurate results using material properties listed in Table 2. The model contained more than 7000 elements in total. A parametric code written in Python was utilized to perform the J-Integral calculation on a specimen whose dimensionless crack length was incremented from 0.15 to 0.8 in steps of 0.01. An example is shown below in Figure 3.

$$G(\alpha) = \frac{\sigma_N^2}{E} Dg(\alpha) = J \qquad Eq.(12)$$

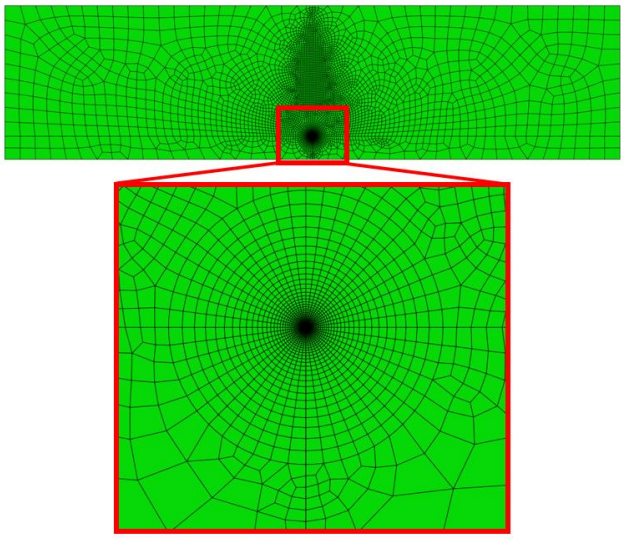

Figure 3 – Example of Abaqus Model for J-Integral Calculation for $\boldsymbol{\alpha = 0.15}$

The results were compared using solutions found by Anderson [8] and Pastor [9] and the comparison is shown below in Figure 4.

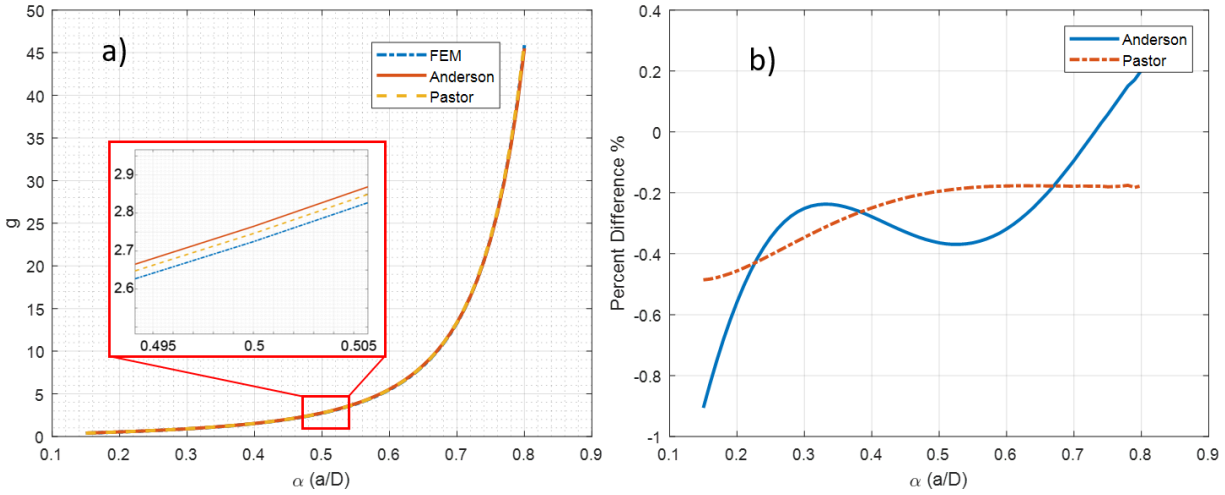


Figure 4a. $g(\alpha)$ comparison between results found by author, Anderson [8] and Pastor [9].
Figure 4b. Percent differences of Anderson and Pastor results compared to FEM.

Moreover, since the J-Integral method models the crack as a line, further verification was needed since using cohesive elements the crack is instead modeled as a band with a finite width. Using the definition of energy release rate, Eq.(13), the total strain energy of the Abaqus model was obtained and numerically differentiated over a short span of dimensionless crack length to verify part of the results obtained using the J-Integral method. Figure 5 below shows the comparison result.

$$\mathcal{G} = \mathcal{G}(u,a) = -\frac{1}{b}\left[\frac{\partial U(u,a)}{\partial a}\right]_u \qquad Eq.(13)$$

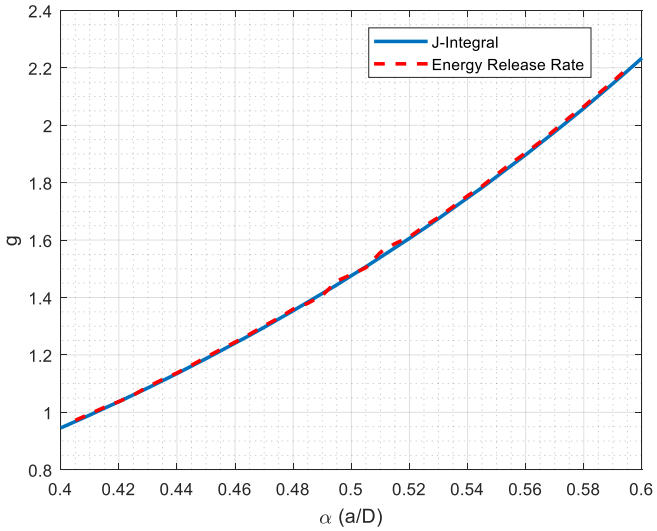


Figure 5 – Comparison for $\boldsymbol{g(\alpha)}$ modeling the crack as a line (J-Integral) and with a finite width (Energy)

## E. MATERIAL PROPERTIES

Once all the parameters are found, the three most important of them were chosen as shown below in Table 1 using the base material properties from Table 2.

Table 1 - Summary of Main Sweeping Parameters

| $G_f/G_F$ | $K_1 / f_t$ | $f_t$ / E | $D$ [mm] | $\delta_{applied}$ [mm] |
|---|---|---|---|---|
| 0.3 | 0.3 | 0.01 | 5 | 0.4 |
| 0.4 | 0.4 | 0.015 | 10 | 0.55 |
| 0.5 | 0.5 | 0.02 | 20 | 0.7 |
| 0.6 | 0.6 | 0.025 | 40 | 1.0 |
| 0.7 | 0.7 | 0.03 | 80 | 1.5 |

Table 2 – Base Material Properties

| | |
|---|---|
| $E$ | 2500 MPa |
| $\nu$ | 0.3 |
| $f_t$ | 50 MPa |
| $G_F$ | 1.6 N/mm |

## METHODOLOGY

This is how the curve are constructed. Given a certain $\alpha$, a parametric python code was written to use the *J-Integral* technique in Abaqus to find $g(\alpha)$ and $g'(\alpha)$ for any given geometry as explained in the previous section. Once these values were found, a $D$ value was chosen (and therefore a corresponding $X$ value as well using Eq. (4)) for each simulation, and the force-displacement response was extracted for geometrically scaled specimens, together with its maximum peak $P_c$. Since nominal stress was used, the peak force was normalized using the following Eq. (14) for three-point bending specimen:

$$\sigma_N = \frac{3P_c S}{2BD^2} \qquad Eq.(14)$$

With the use of nominal stress, the $Y$ value was found using Eq.(5). At this point, a simulation scheduler was written using Python to sweep all the wanted parameters and use the workflow described above to extract both $X$ and $Y$ components to be used in the parametric space. Figure 6 below shows the general nomenclature of a three point bending specimen whose width (D) is four times the specimen length (W).

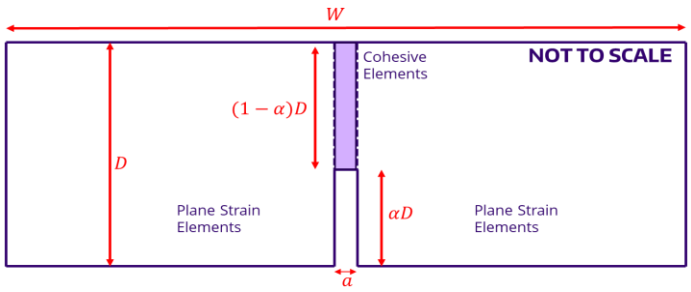


Figure 6 – 3PTB4 General Nomenclature Specimen

For these simulations, a band of constant size (0.02mm x 0.02mm) cohesive elements (COH2D4) were used to model the propagation of the crack. The size of such elements was chosen to have at least 80 elements in the fracture process zone (FPZ). For the rest of the specimen, plane strain elements (CPE4R) were used as shown below in Figure 7. For specimens whose width dimension was lower than 20mm, an implicit solver was used; while to run larger specimens, an explicit solver was used together with semiautomatic mass scaling ($\Delta t = 1e\text{-}6$ seconds), enhanced hourglass control and distortion control. Kinetic energy for the explicit simulations was systematically checked to be at least two orders of magnitude lower than the total internal kinetic energy.

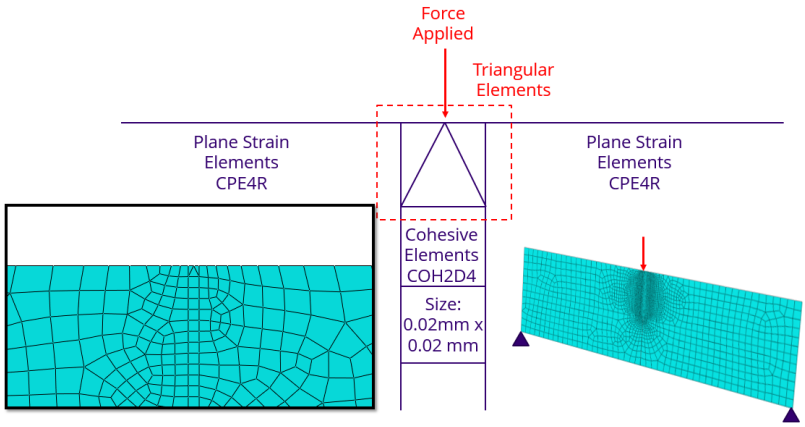


Figure 7 – Abaqus Model Specifications

## RESULTS

### A. LINEAR CASE

In order to first verify and compare the results obtained with the results available in the literature, a linear cohesive case ($\gamma = 1$) was chosen and compared with results obtained by Cusatis [4]. Figure 8 below shows the results of five geometrically scaled specimen whose width is specified in the legend.

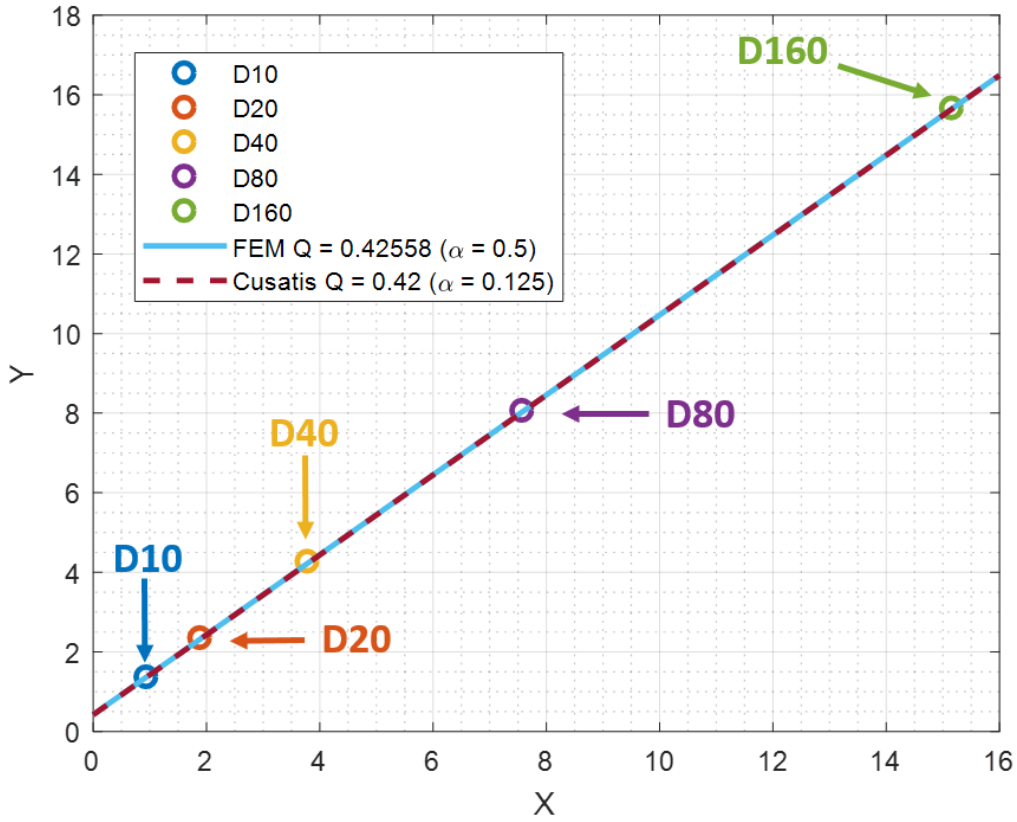


Figure 8 – Comparison with Cusatis [2] to verify linear cohesive behavior

The intercept, listed as "Q" in the legend of the figure above, obtained from the linear regression analysis exactly matched the results of Cusatis [4].

## B. BILINEAR CASES

Preliminary results shown to be consistent with the results found by Cusatis [4] for the case of $K_1/f_t = 0.25$, $f_t/E = 0.02$, and $G_f/G_F = 0.5$, but the work presented is much more extended for all the parameters as shown example in Figure 9.

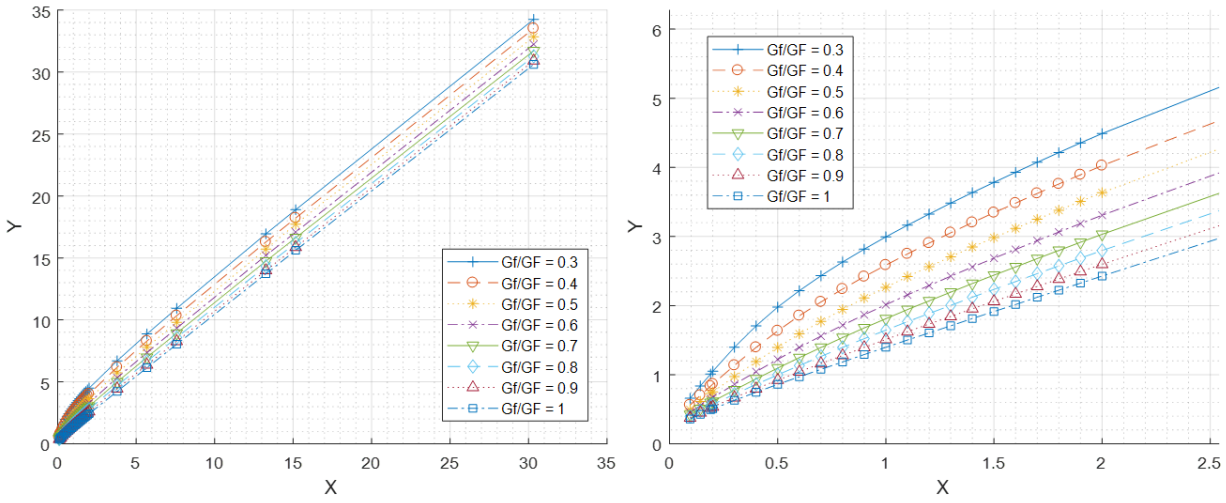


Figure 9 - Parametric Simulations for $\boldsymbol{K_1 / f_t = 0.25}$, $\boldsymbol{f_t/E = 0.02}$ and multiple values of $\boldsymbol{G_f/G_F}$

All the points found were fitted by asymptotic matching using a semi-empirical formulation, using Eq.(15a) to Eq.(15c).

$$Y(X) = \left(\frac{1}{1-1/\beta^m}\right)^{\frac{1}{m}} \Psi(X) \cdot \left\{1 + \left[\frac{\Psi(X)}{\chi(X)}\right]^m \cdot \left(\frac{1}{1-1/\beta^m}\right)\right\}^{-\frac{1}{m}} \qquad Eq.(15a)$$

$$\Psi(X) = \frac{G_F}{G_f} X + \frac{1 + 0.44a\sqrt{(G_F/G_f)\cdot X}}{9(1-\alpha)^4 g'(\alpha) + a\sqrt{(G_F/G_f)\cdot X}} \qquad Eq.(15b)$$

$$\chi(X) = X + \frac{1 + \xi a\sqrt{X}}{[9(1-\alpha)^4 g'(\alpha)]/\beta + a\sqrt{X}} \qquad Eq.(15c)$$

Where $\Psi(X)$ is the part of the equation that drives the fitting of the first asymptote while $\chi(X)$ drives the fitting of the second asymptote. $\Psi(X)$ and $\chi(X)$ were designed assuming a power law and the exponent $m$ and $\beta$ were properly placed in order to drive properly the transition behavior.

Knowing the literature values for the lower and upper asymptotes [2],[3], the solution is based on the four different parameters $a, \beta, m, \xi$. For example, for the case of $K_1/f_t = 0.25$, $f_t/E = 0.02$, and $G_f/G_F = 0.3$ Figure 10 shows the following results followed by Table 3 with the parameters values found using the method of Nonlinear Least Squares using Matlab [10] coupled with a robust Least Absolute Residuals (LAR) method.

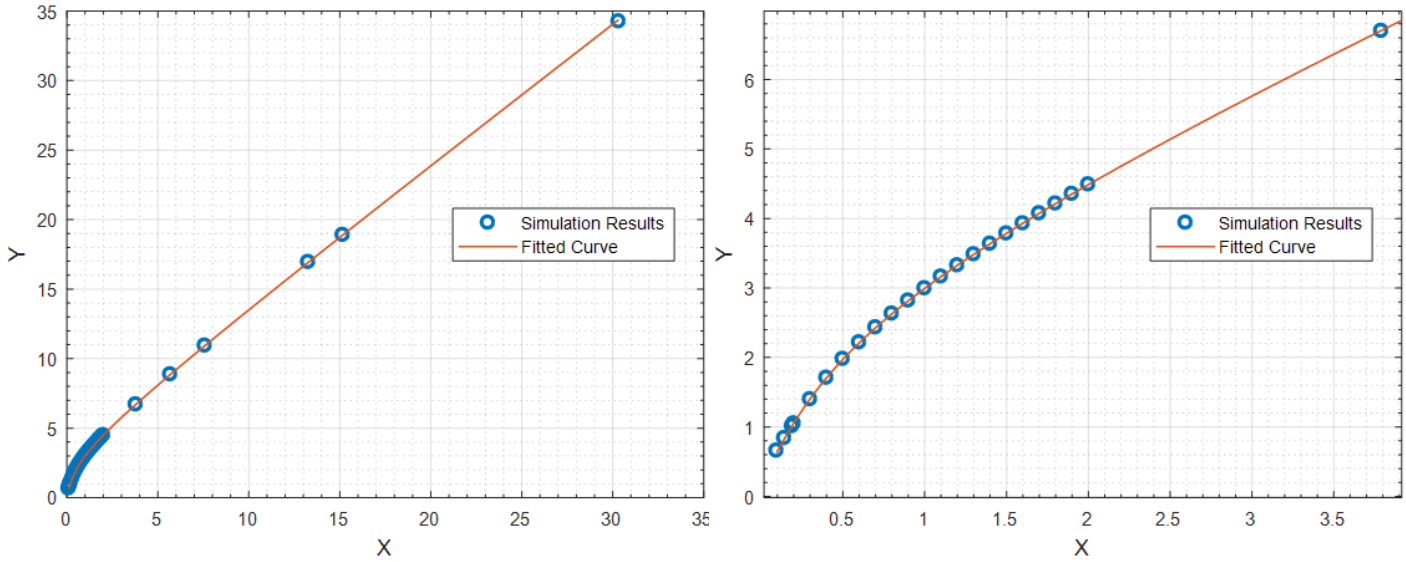


Figure 10 - Fitting Results for $\boldsymbol{K_1 / f_t = 0.25}$, $\boldsymbol{f_t/E = 0.02}$ and $\boldsymbol{G_f/G_F = 0.3}$

Table 3 - Fitting Parameters results using Nonlinear Least Square method and LAR

| | |
|---|---|
| $a$ | 5.97 |
| $\beta$ | 1.10 |
| $m$ | 4.30 |
| $\xi$ | 5.19 |
| $R^2$ | 1.0000 |

### C. PARAMETERS EVOLUTION

While each set of simulation can be fitted by itself with different values of parameters, it is of interest study the evolution of such parameters so that they could be fit and used to better estimate fracture properties.

1. $K_1/f_t = 0.25, f_t/E = 0.02$

Figure 11 below shows how the chosen parameters evolve as a function of energy ratio $\gamma$.

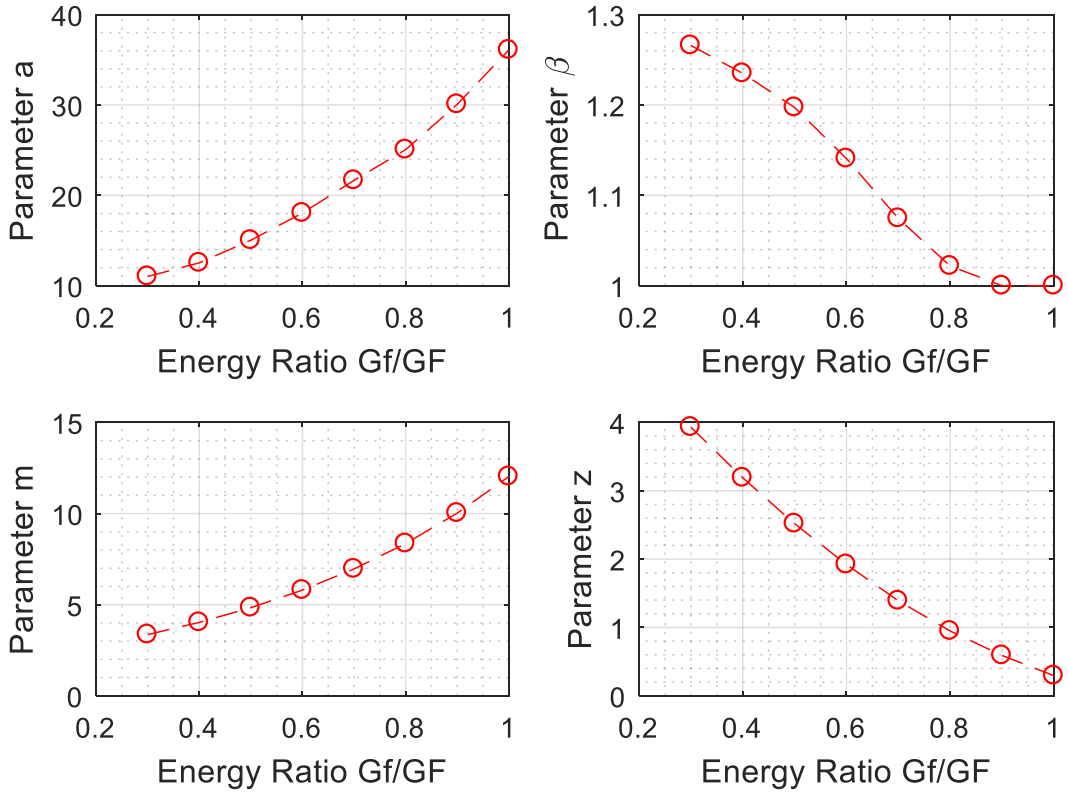


Figure 11 – Parameters evolution for $\boldsymbol{K_1/f_t = 0.25}$ , $\boldsymbol{f_t/E = 0.02}$

At this point these curves can be fitted using either polynomials or exponential equations. For the case above the parameters can be fitted into the following equations:

$$a\left(\frac{G_f}{G_F}\right) = 6.385 \cdot e^{1.726\frac{G_f}{G_F}} \quad | \quad R^2 = 0.9991 \qquad Eq.(16a)$$

$$\beta\left(\frac{G_f}{G_F}\right) = -0.1058\left(\frac{G_f}{G_F}\right) + 1.117 \quad | \quad R^2 = 0.9576 \qquad Eq.(16b)$$

$$m\left(\frac{G_f}{G_F}\right) = 1.943 \cdot e^{1.823\frac{G_f}{G_F}} \quad | \quad R^2 = 1 \qquad Eq.(16c)$$

$$\xi\left(\frac{G_f}{G_F}\right) = 0.2288\left(\frac{G_f}{G_F}\right)^2 - 1.274\left(\frac{G_f}{G_F}\right) + 1.648 \quad | \quad R^2 = 1 \qquad Eq.(16d)$$

2. $K_1/f_t = 0.50, f_t/E = 0.02$

Similarly:

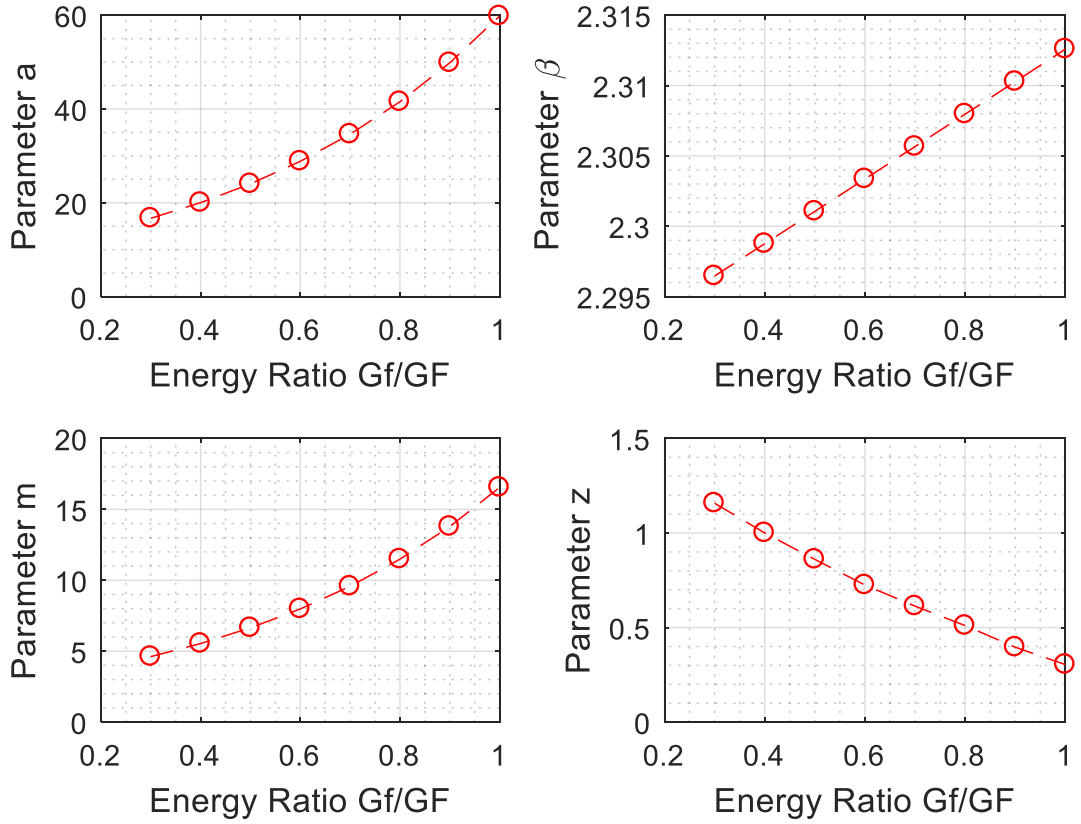


Figure 12 – Parameters evolution for $\boldsymbol{K_1/f_t = 0.50}$ , $\boldsymbol{f_t/E = 0.02}$

Where the parameters can be fitted using Eq.(17) below:

$$a\left(\frac{G_f}{G_F}\right) = 9.659 \cdot e^{1.823\frac{G_f}{G_F}} \quad | \quad R^2 = 1 \qquad Eq.(17a)$$

$$\beta = 2.305 \qquad Eq.(17b)$$

$$m\left(\frac{G_f}{G_F}\right) = 2.672 \cdot e^{1.823\frac{G_f}{G_F}} \quad | \quad R^2 = 1 \qquad Eq.(17c)$$

$$\xi\left(\frac{G_f}{G_F}\right) = 0.0295\left(\frac{G_f}{G_F}\right)^2 - 0.2961\left(\frac{G_f}{G_F}\right) + 0.6701 \quad | \quad R^2 = 0.9997 \qquad Eq.(17d)$$

3. $K_1/f_t = 0.75, f_t/E = 0.02$

Finally:

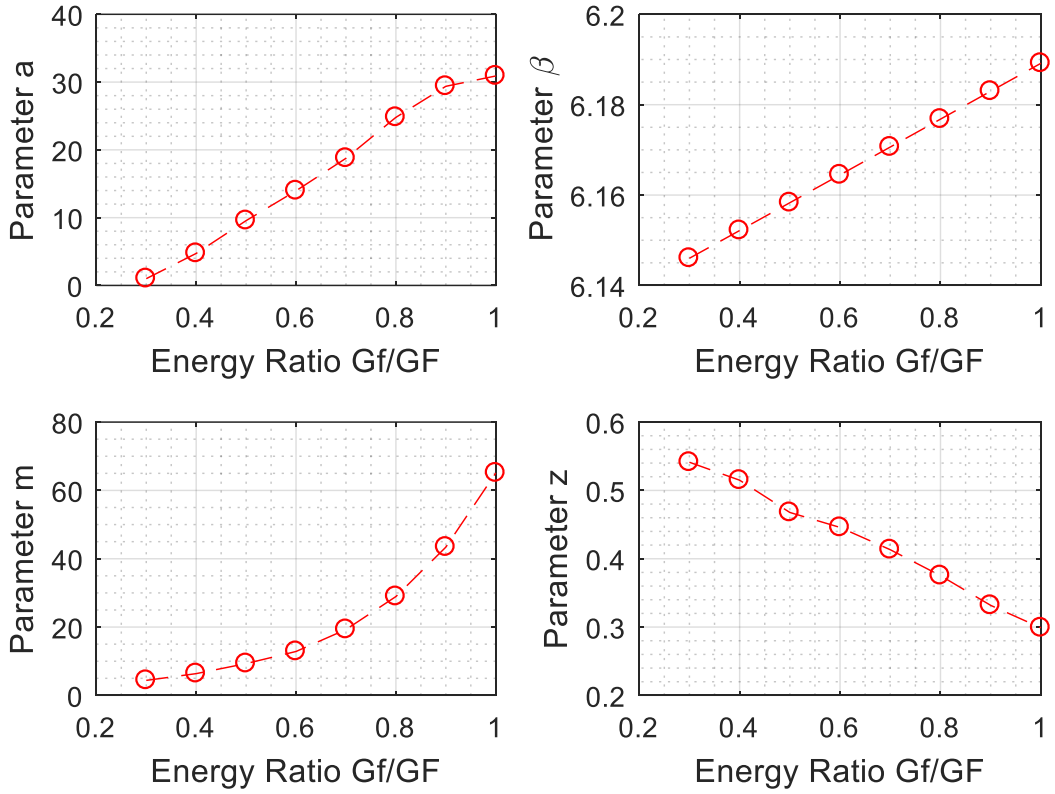


Figure 13 – Parameters evolution for $\boldsymbol{K_1/f_t = 0.75}$ , $\boldsymbol{f_t/E = 0.02}$

Where the parameters can be fitted using Eq.(18) below:

$$a\left(\frac{G_f}{G_F}\right) = 45.61\left(\frac{G_f}{G_F}\right) - 13.01 \quad | \quad R^2 = 0.9907 \qquad Eq.(18a)$$

$$\beta = 6.17 \qquad Eq.(18b)$$

$$m\left(\frac{G_f}{G_F}\right) = 1.194 \cdot e^{3.995\frac{G_f}{G_F}} \quad | \quad R^2 = 0.9997 \qquad Eq.(18c)$$

$$\xi\left(\frac{G_f}{G_F}\right) = -0.3479\left(\frac{G_f}{G_F}\right) + 0.6497 \quad | \quad R^2 = 0.995 \qquad Eq.(18d)$$

## CONCLUSION

In conclusion, the results of this study made clear that size effect is indeed strongly affected not only by the total fracture energy $G_F$, but also all the other parameters of the cohesive law: $f_t$, $G_f$, $\gamma$, and $K_1$. This is substantially different from LEFM which instead assumes that fracturing behavior is governed by the fracture energy only. These results also agree with recent [1],[2] and older [11] studies, which also state that the shape of the cohesive law does play a significant role in the overall behavior of the structure.

Future studies and further simulations will focus on the application of the proposed size effect equation for the characterization of the main parameters of the cohesive law in composites and nanocomposites. The estimated parameters will be readily used for the calibration and validation of proper cohesive laws for composites.

## References


[1] Salviato, M., Kirane, K., Ashari, S.E., Bažant, Z.P. and Cusatis, G., 2016. Experimental and numerical investigation of intra-laminar energy dissipation and size effect in two-dimensional textile composites. Composites Science and Technology, 135, pp.67-75.

[2] Mefford, C.H., Qiao, Y. and Salviato, M., 2017. Failure behavior and scaling of graphene nanocomposites. Composite Structures, 176, pp.961-972.

[3] Qiao, Y., Salviato, M., 2018. A Cohesive Zone Modeling Study on the Fracturing Behavior of Thermoset Polymer Nanocomposites. Proceedings to 33rd Annual Technical Conference, 18th US-Japan Conference on Composite Materials ASTM D30.

[4] Cusatis, G. and Schauffert, E.A., 2009. Cohesive crack analysis of size effect. Engineering Fracture Mechanics, 76(14), pp.2163-2173.

[5] Rice, J.R., 1968. A path independent integral and the approximate analysis of strain concentration by notches and cracks. Journal of applied mechanics, 35(2), pp.379-386.J Integral

[6] Hibbett, Karlsson and Sorensen, 1998. ABAQUS/standard: User's Manual (Vol. 1). Hibbitt, Karlsson & Sorensen.

[7] Barsoum, R.S., 1976. A degenerate solid element for linear fracture analysis of plate bending and general shells. International Journal for Numerical Methods in Engineering, 10(3), pp.551-564.

[8] Anderson, T.L., 2017. *Fracture mechanics: fundamentals and applications*. CRC press.

[9] Guinea, G.V., Pastor, J.Y., Planas, J. and Elices, M., 1998. Stress intensity factor, compliance and CMOD for a general three-point-bend beam. *International Journal of Fracture*, *89*(2), pp.103-116.

[10] The MathWorks, Inc., "Matlab 2016b," The MathWorks, Inc., Natick, 2016.

[11] Bažant, Z.P., 1984. Size effect in blunt fracture: concrete, rock, metal. Journal of Engineering Mechanics, 110(4), pp.518-535.